Monthly Notices
of the
ROYAL ASTRONOMICAL SOCIETY

MNRAS **460,** 1614–1624 (2016)
Advance Access publication 2016 May 9

doi:10.1093/mnras/stw1088

Supernova 2014J at M82 – II. Direct analysis of a middle-class Type Ia supernova

Patrick Vallely,[1] M. E. Moreno-Raya,[2] E. Baron,[1,3]★ Pilar Ruiz-Lapuente,[4,5] I. Domínguez,[6] Lluís Galbany,[7,8] J. I. González Hernández,[9,10] J. Méndez,[11] M. Hamuy,[8,7] A. R. López-Sánchez,[12,13] S. Catalán,[14] E. Cooke,[15] C. Fariña,[11] R. Génova-Santos,[9,10] R. Karjalainen,[11] H. Lietzen,[9,10] J. McCormac,[14] F. Riddick,[11] J. A. Rubiño-Martín,[9,10] I. Skillen,[11] V. Tudor[11] and O. Vaduvescu[11]

[1]*Homer L. Dodge Department of Physics and Astronomy, University of Oklahoma, 440 W. Brooks, Rm 100, Norman, OK 73019-2061 USA*
[2]*Departamento de Investigación Básica, CIEMAT, Avda. Complutense 40, E-28040 Madrid, Spain*
[3]*Hamburger Sternwarte, Gojenbergsweg 112, D-21029 Hamburg, Germany*
[4]*Instituto de Física Fundamental, Consejo Superior de Investigaciones Cientfficas, c/. Serrano 121, E-28006 Madrid, Spain*
[5]*Institut de Ciéncies del Cosmos (UB-IEEC), c/. Martí i i Franqués 1, E-08028 Barcelona, Spain*
[6]*Universidad de Granada, E-18071 Granada, Spain*
[7]*Millennium Institute of Astrophysics, Universidad de Chile, Chile*
[8]*Departamento de Astronomía, Universidad de Chile, Santiago, Chile*
[9]*Instituto de Astrofísica de Canarias, E-38200 La Laguna, Tenerife, Spain*
[10]*Departmento de Astrofísica, Universidad de La Laguna (ULL), E-38206 La Laguna, Tenerife, Spain*
[11]*Isaac Newton Group of Telescopes, Apto. 321, E-38700 Santa Cruz de la Palma, Canary Islands, Spain*
[12]*Australian Astronomical Observatory, PO BOX 296, Epping, NSW 1710, Australia*
[13]*Department of Physics and Astronomy, Macquarie University, NSW 2109, Australia*
[14]*Department of Physics, University of Warwick, Coventry CV47AL, UK*
[15]*School of Physics and Astronomy, University of Nottingham, University Park, Nottingham NG7 2RD, UK*

Accepted 2016 May 5. Received 2016 May 4; in original form 2015 December 8

ABSTRACT

We analyse a time series of optical spectra of SN 2014J from almost two weeks prior to maximum to nearly four months after maximum. We perform our analysis using the SYNOW code, which is well suited to track the distribution of the ions with velocity in the ejecta. We show that almost all of the spectral features during the entire epoch can be identified with permitted transitions of the common ions found in normal supernovae (SNe) Ia in agreement with previous studies. We show that 2014J is a relatively normal SN Ia. At early times the spectral features are dominated by Si II, S II, Mg II, and Ca II. These ions persist to maximum light with the appearance of Na I and Mg I. At later times iron-group elements also appear, as expected in the stratified abundance model of the formation of normal Type Ia SNe. We do not find significant spectroscopic evidence for oxygen, until 100 d after maximum light. The +100 d identification of oxygen is tentative, and would imply significant mixing of unburned or only slight processed elements down to a velocity of 6000 kms^{-1}. Our results are in relatively good agreement with other analyses in the infrared. We briefly compare SN 2011fe to SN 2014J and conclude that the differences could be due to different central densities at ignition or differences in the C/O ratio of the progenitors.

Key words: supernovae: general – supernovae: individual: 2014J, 2011Fe.

1 INTRODUCTION

SN 2014J, located in M82 only a 3.3 Mpc away (Foley et al. 2014), is the closest SN Ia observed in the last 40 yr. As the nearest modern SN Ia, SN 2014J has been extremely well observed: in γ-rays (Churazov et al. 2014; Diehl et al. 2014), X-rays (Margutti et al. 2014), by *Hubble Space Telescope* (Foley et al. 2014; Kelly et al. 2014), optical (Amanullah et al. 2014; Ashall et al. 2014; Goobar et al. 2014; Nielsen et al. 2014) at high resolution (Welty et al. 2014; Graham et al. 2015; Jack, Baron & Hauschildt 2015; Ritchey et al. 2015), near-infrared (near-IR; Friesen et al. 2014;

★ E-mail: baron@ou.edu

Marion et al. 2015), mid-IR (Johansson et al. 2014; Telesco et al. 2015), polarimetry (Kawabata et al. 2014), with rapid photometry (Siverd et al. 2015), and in radio (Pérez-Torres et al. 2014).

In Galbany et al. (2016, henceforth Paper I), we present a long-time baseline set of optical spectroscopy and we analysed the data set using wavelength matching to obtain line identifications and velocities. By the term wavelength matching, we mean that no modelling of the spectra was performed, the line IDs were simply made by matching the wavelength of an observed feature to known wavelengths of characteristic lines. Here, we take that analysis one step further using the parametrized synthetic-spectrum code SYNOW (Jeffery & Branch 1990; Branch, Baron & Jeffery 2003). In the SYNOW framework, we model the observed spectra, identify the line features, and determine the photospheric velocity and the velocity extent of the ions of SN 2014J at each epoch.

The SYNOW code is based on simple assumptions, described in more detail below. A synthetic spectrum consists of blended P Cygni profiles (emission component, blueshifted absorption component) superimposed on a continuum. SYNOW does not do continuum transport, it does not solve rate equations, and it does not calculate ionization ratios. Its main function is to take multiple line scattering into account so that it can be used in an empirical spirit to make line identifications and estimate the velocity at the photosphere (or pseudo-photosphere), and the velocity interval within which each ion is detected. These quantities provide constraints on the composition structure of the ejected matter.

As described above, SYNOW is a parametrized line-scattering code that includes the effects for multiple scattering. An opaque photosphere illuminates the atmosphere with a blackbody. The velocity is homologous, $v \propto r$, and the photosphere is at a velocity coordinate $v_{\rm ph}$. The source function is taken to be that of resonance scattering $S = W(r)I_{\rm ph}$, where $I_{\rm ph}$ is the intensity from the photosphere and

$$W = \frac{1}{2}\left\{1 - \sqrt{1 - (\frac{r_{\rm ph}}{r})^2}\right\}$$

is the dilution factor (Mihalas 1978), and $r_{\rm ph}$ is the photospheric radius.

Lines are treated in the Sobolev approximation. The Sobolev optical depth, $\tau_{\rm sob}$, is a local quantity, given by

$$\tau_{\rm sob} = \left(\frac{\pi e^2}{m_e c}\right) f_{\rm o} n_{\rm l}(1 - \frac{g_{\rm l} n_{\rm u}}{g_{\rm u} n_{\rm l}})\lambda_0 / \frac{{\rm d}v}{{\rm d}r},$$

where l designates the lower level of the transition, u the upper level, $f_{\rm o}$ is the oscillator strength of the line, $n_{\rm l}$ and $n_{\rm u}$ are the occupation numbers of the levels and $g_{\rm l}$ and $g_{\rm u}$ are the statistical weights of the levels (Jeffery & Branch 1990).

In SYNOW, a reference line is chosen for each ion and $n_{\rm l}$ is assumed to vary as e^{-v/v_e}. v_e is the density scalefactor in units of kms^{-1} and its value determines the velocity extent of the absorption trough. Thus, τ for the reference line is given as $\tau(v) = \tau e^{-v/v_e}$, where τ is the value of the Sobolev optical depth where the ion begins, usually at the photosphere, $v_{\rm ph}$, but the line may be detached and begin at a velocity $v_{\rm min_e}$. Everything else about the ion is assumed to be given by the Boltzmann formulae with an ion temperature $T_{\rm exe}$. For more information about the SYNOW code see Jeffery & Branch (1990) and Branch et al. (2004, 2005, 2007). The specific values optimized by eye are $v_{\rm ph}$, $T_{\rm bb}$, $T_{\rm exe}$, and the velocity and optical depth of each ion. Values for each input parameter are determined by manually varying them and examining the resultant spectra until the best possible match by eye is obtained. These parameters are determined by the quality of the model. $v_{\rm ph}$ is determined by global constraints across all line shapes. $v_{\rm min_e}$ is used only if detachment is deemed to be required after first trying hard without detached lines. $T_{\rm exe}$ is not a terribly important parameter and its value is pretty much kept at the default value unless there is a need to have more or less abundance in upper or lower states of a given ion. The error estimates for τ were obtained by varying the parameter values and choosing an acceptable range as judged by eye.

While this by eye pattern matching is standard in the community (see, for example, Parrent et al. 2012, and references therein), one could go further in terms of fitting and try to construct some form of complex likelihood combined with Markov Chain Monte Carlo, it would be overkill for the intended purpose of ion identification and velocity extent that is the goal of this and similar analyses. To our knowledge, it has never been done and is beyond the scope of this work.

The spectral epochs range from almost two weeks pre-maximum to nearly three months post-maximum with wavelengths from roughly 3500 to 9500 Å. We take the time of maximum to be 2014 February 1 (Paper I). The spectra are corrected to account for being heavily reddened by dust in the host galaxy as well as for foreground extinction. We use the reddening values found by Goobar et al. (2014). We use this multi-epoch spectral data set to identify the ions in the spectra as a function of time and analyse their velocity extent. Since Type Ia supernovae play such an important role as cosmological probes, their progenitor system is uncertain and the explosion mechanism is not well understood (for recent reviews see Hillebrandt et al. 2013; Maoz, Mannucci & Nelemans 2014; Ruiz-Lapuente 2014), detailed analyses of the explosion products of well-observed supernovae (SNe) Ia are particularly useful to gain insight into these unresolved questions. A good introduction to the analysis of supernova spectra is given in Parrent, Friesen & Parthasarathy (2014, and references therein). In Section 2, we identify the ions and their velocity extent for epochs up to Day −4.6. In Section 3, we identify the ions and their velocity extent for epochs near maximum light, up to Day +12.4. Section 4 studies the epochs up until Day +22.5, and Section 5 examines late epochs between Day +33.4 and +99.1. In Section 6, we discuss the velocities we have obtained for the photosphere and compare those to what others have found for SN 2014J and other Branch normal supernovae. Section 7 compares the results we have found for SN 2014J directly with those of SN 2011fe and describes possible reasons for similarities and differences between the two supernovae. Finally, in Section 8 we recap and present our conclusions.

2 PRE-MAXIMUM SPECTRA

Observational details of all of the data used for this work can be found in Paper I. Our earliest observed spectrum was obtained on January 23 (Day −9.6), and we examine a total of six spectra obtained between January 23 (Day −9.6) and January 28 (Day −4.6).The pre-maximum spectra all show standard SNe Ia features: Si II λ6355, Si II λ5972 S II absorption centred at 5300 Å, Mg II absorption centred at 4400 Å as well as 7600 Å (Mg II λλ7889.9), Mg I λλ5178.3, and Ca II H+K (absorption centred around 3700 Å) and the IR triplet with absorption centred at 8200 Å. In this time period, there is only minimal evolution. The SYNOW spectra include lines of five ions: Mg I, Mg II, Si II, S II, and Ca II. In addition to the photospheric component, Ca II has a detached high-velocity component, and a detachment velocity of $v_{\rm min_e} = 23\,000$ kms^{-1} is used for all of the pre-maximum models. Values of $v_{\rm phot} = 14\,000$ kms^{-1} and $T_{\rm exe} = 10\,000$ K are used for all ions. A complete list of input parameters can be found in Table 1.

Table 1. SYNOW parameters for pre-maximum spectra model.

Date	$v_{\rm phot}$	$T_{\rm bb}$	$T_{\rm exe}$	Pre-maximum SYNOW Parameters												
				Mg I		Mg II		Si II		S II		Ca II		HV Ca II		
				τ	v_e	τ	v_e	τ	v_e	τ	v_e	τ	v_e	τ	v_e	$v_{\rm min_e}$
Jan 23(−9.6)	14	14	10	1 ± 0.1	2	2.5 ± 0.5	2	2 ± 0.2	3	1.3 ± 0.1	2	15 ± 2.5	3	10 ± 2	3	23
Jan 24(−8.5)	14	14	10	1 ± 0.1	2	2.5 ± 0.5	2	2 ± 0.2	3	1.3 ± 0.1	2	15 ± 2.5	3	10 ± 2	3	23
Jan 25(−7.4)	14	17	10	0.8 ± 0.1	2	2 ± 0.4	2	3 ± 0.3	2	1 ± 0.1	2	20 ± 4	3	10 ± 2	3	23
Jan 26(−6.5)	14	18	10	1 ± 0.1	2	2 ± 0.4	2	3 ± 0.3	2	1 ± 0.1	2	25 ± 5	3	10 ± 2	3	23
Jan 27(−5.4)	14	22	10	1 ± 0.1	2	2 ± 0.4	2	4 ± 0.4	2	1.2 ± 0.1	2	25 ± 5	3	10 ± 2	3	23
Jan 28(−4.6)	14	24	10	1 ± 0.1	2	2 ± 0.4	2	4 ± 0.4	2	1.7 ± 0.2	2	35 ± 7	3	20 ± 3	3	23

The upper panel of Fig. 1 shows the observed spectrum obtained on January 24 (Day −8.5) compared with the SYNOW model. Here, high-velocity Ca is modelled with a detached high-velocity component.

The middle panel of Fig. 1 shows the observed spectrum obtained on January 28 (Day −4.6) and the SYNOW model, and the lower panel shows the flattened spectra, where the spectra have been normalized by the local (pseudo-) continuum in that wavelength region using the prescription of Jeffery et al. (2007). The Ca II detached high-velocity component persists through this epoch. Flattened spectra are often presented in the literature, so we include them for the benefit of readers who are used to seeing them. The models were calculated on the original, unflattened spectra.

The photospheric velocity remains constant throughout this period, the Mg II lines strength is constant (that is, τ doesn't change), Si II strengthens, S II strengthens, photospheric Ca II lines get stronger, and the high-velocity feature is present throughout. While Ca H+K is at the blue edge of these spectra, it is a distinctive and relatively unblended feature and the Ca II IR triplet also provides a constraint.

We do not find strong spectroscopic evidence for O I λ7774, as O I is not used in the SYNOW model, whereas abundance tomography finds that the high-velocity ejecta is dominated by oxygen (Ashall et al. 2014). We will discuss this discrepancy in more detail in Section 8.

3 NEAR-MAXIMUM SPECTRA

Maximum light occurred on 2014 February 1, and we examine six spectra obtained between February 4 (Day +2.3) and February 14 (Day +12.4). SYNOW spectra include lines of the following ions: Na I, Mg I, Mg II, Si II, Si III, S II, and Ca II. A complete list of input parameters is given in Table 2. Values of $v_{\rm phot} = 12\,000$ kms^{-1}, and $T_e = 10\,000$ K are used for all ions except for the February 14 (Day +12.4) spectra, in which a value of $v_{\rm phot} = 11\,000$ kms^{-1} is used. The line identifications remain the same as in Section 2 with the addition of Na I D (with absorption centred at 5700 Å). The S II absorption feature declines steadily with time. In normal SNe Ia, the S II W feature is distinct and relatively easy to identify. The detached high-velocity Ca II component is no longer present. For spectra that don't cover Ca II, it was not reported in the table. The increase in strength of Ca II, indicates the ejecta are cooling and Ca II becomes strong. The Na I line is likely, but the large τ found for the February 6 (Day +4.2) spectrum is due to the dichroic break in the observed spectrum. Comparing with Ashall et al. (2014), our results are somewhat different, by this time they find a significant amount of Fe II, which they take as evidence for ^{56}Ni above the photosphere, we do not find strong evidence for this. Na D are typically identified on core normal (or close to core normal) SNe Ia about one week post-maximum light (Branch et al. 2008).

The upper-left panel of Fig. 2 shows the observed spectrum obtained on February 4 (Day +2.3) and the SYNOW model. The blue and red arms of the observed spectrum were matched at 6000 Å. The match was simply to remove the red (blue) wing of the blue (red) spectra due to the low transmission at those wavelengths. There was no disagreement in the flux calibrations, but in this way we could treat both spectra as if it was a single spectrum. Note that this is clearly shown in fig. 3 of Paper I, e.g. spectra at epoch −7.4 d was matched at 7300 Å, and spectra at epoch +2.3d at 6000 Å. In the first case (−7.4 d) the two spectra have different resolutions (3.30 and 0.49 Å pix^{-1}), while in the second (+2.3 d) they had the same resolution (0.53 Å pix^{-1}) and the effect is clearly not visible.

The upper-right panel of Fig. 2 shows the observed spectrum obtained on February 5 (Day +3.3) and the SYNOW model. A value of $v_{\rm phot} = 12\,000$ kms^{-1} is used. Si III is now used in the model, to help with the absorption produced by the Si III λλ4425.3 line and the absorption in the Na I D trough produced by the Si III λλ5707.5 line. Since it is only used to help with absorption in blended features, the Si III identification is tentative.

The lower-left panel of Fig. 2 shows the observed spectrum obtained on February 12 (Day +10.5) and the SYNOW model. It exhibits Mg I absorption centred at 5000 Å and Mg II absorption centred at 7600 and 8900 Å. A value of $v_{\rm phot} = 12\,000$ kms^{-1} is used.

The lower-right panel shows the observed spectrum obtained on February 14 (Day +12.4) and the SYNOW model. This is nearly identical to the Day +10.5 model, but with Si III, and weaker Si II.

Looking at the four panels in Fig. 2, it appears as if the model of the Mg I doublet degrades with epoch from February 4 to 12, however, in reality the two features seen in absorption at 4750 and 5000 Å are stronger in the last epoch and thus, the Mg I identification on day +12.4 is provisionary. That is, while we believe that the feature is produced to some extent by Mg I, without determining the other ions that produce the blended feature we cannot be sure of the velocity extent of Mg I.

4 POST-MAXIMUM SPECTRA

Six spectra were obtained between February 19 (Day +17.4) and February 26 (Day +24.5). The post-maximum spectra share the same general features – Si II absorption centred at 6100 Å, Mg II absorption centred at 7600 Å, Ca II absorption centred at 8200 Å, Fe II absorption centred at 8900 Å, and Na I and Si III absorption centred at 5600 Å, with some variation. Since the Si III is there just to help in the Na I D trough, and it is physically unlikely to have such highly excited ions at this stage, we regard the Si III as weak at this epoch. The SYNOW spectra include lines of seven ions: Na I, Mg I, Mg II, Si II, Si III, Ca II, and Fe II. Values of $v_{\rm phot} = 11\,000$ kms^{-1}

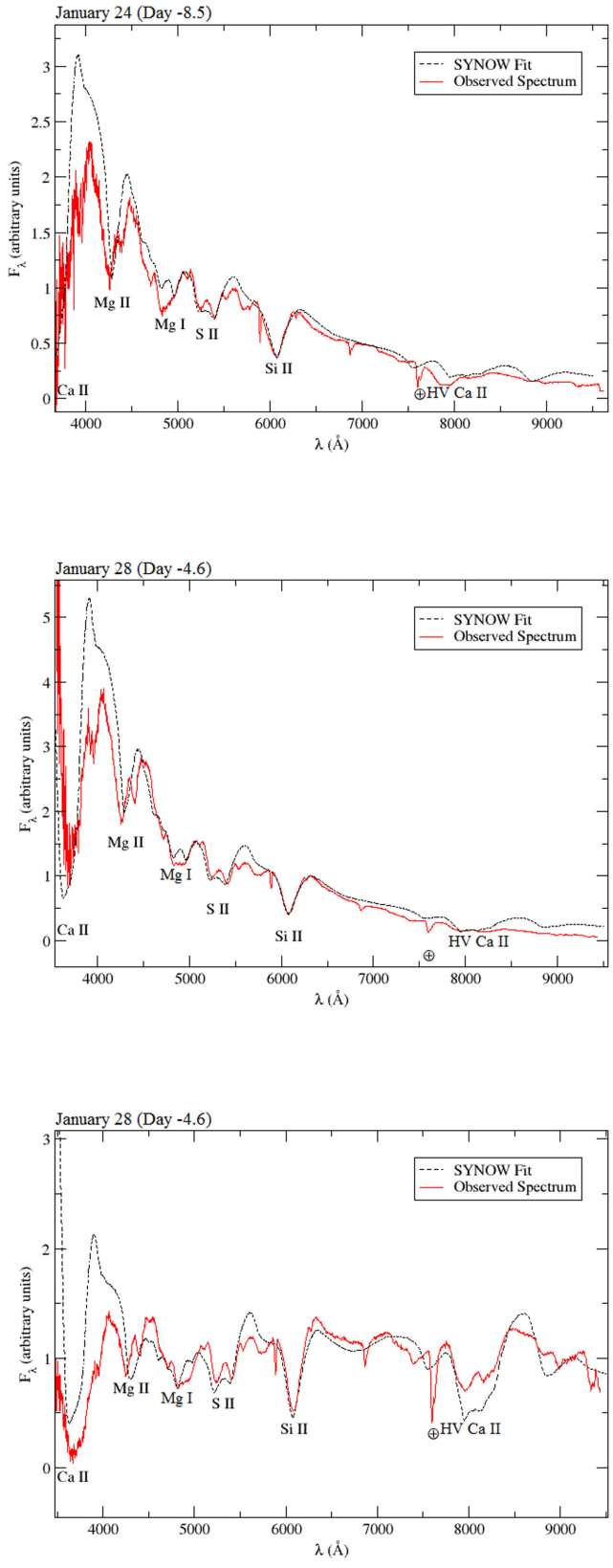

Figure 1. The observed spectra and SYNOW model representative of the pre-maximum epoch. The upper panel shows the January 24 (Day −8.5) spectra, the middle panel shows the January 28 (Day −4.6) spectra, and the bottom panel shows the flattened January 28 (Day −4.6) spectra.

and $T_e = 10\,000$ K are used for all ions except for the February 24 (Day +22.5) and February 26 (Day +24.5) spectra, where $v_{\rm phot}$ is reduced to 10 000 kms^{-1}. Table 3 lists the input parameters.

The upper-left panel of Fig. 3 shows the observed spectrum obtained on February 19 (Day +17.4) and the SYNOW model, and the upper-right panel shows the flattened spectra. The synthetic spectrum is a decent reproduction of the observations. It has several prominent features: Si II absorption centred at 6100 Å, Na I absorption centred at 5700 Å, Mg I absorption centred at 5000 Å, Mg II absorption centred at 7600 and 8900 Å, and Ca II absorption centred at 8200 Å. A value of $v_{\rm phot} = 11\,000$ kms^{-1} is used.

The lower-left panel of Fig. 3 shows the observed spectrum obtained on February 21 (Day +19.5) and the SYNOW model. This epoch marks the beginning of the Fe II presence that characterizes the later synthetic spectra with a value of $\tau = 3.0$ and the continued presence of the blackbody bump around 7000 Å. A value of $v_{\rm phot} = 11\,000$ kms^{-1} is used.

The lower-right panel shows the observed spectrum obtained on February 24 (Day +22.5) and the SYNOW model. As is characteristic of the post-maximum spectra, the synthetic spectrum is decent. Fe II is growing in strength to $\tau = 6.0$. A value of $v_{\rm phot} = 10\,000$ kms^{-1} is used.

5 LATE SPECTRA

The final spectrum we examined was obtained on May 11 (Day +99.1), and we have eight spectra obtained between March 6 (Day +33.4) and May 11 (Day +99.1). The late spectra share some general features – Na I absorption centred at 5600 Å, Mg II absorption centred at 7600 Å, Ca II absorption centred at 8200 Å, Co II absorption centred at 5000 and 6400 Å, and Fe II absorption centred at 8900 Å – although with far more variation than observed in the earlier epochs. Their SYNOW spectra include lines of seven ions: Na I, Mg I, Mg II, Ca II, Fe II, Co II, and Ni II. The $v_{\rm phot}$ values used decrease from 9000 to 6000 kms^{-1} as the spectra age, and $T_{\rm exe} = 6000$ K is used for the four latest spectra. A complete list of input parameters can be found in Table 4.

These later spectra where we see much deeper into the ejecta are also likely indicating that our exponential density parametrization is too simplistic for the entire ejecta. Our models are very smooth, whereas the observations show more complex line shapes. The ejecta density profile is possibly more complex, which may lead to the observed line shapes, but to introduce more complex density parameterizations is beyond the scope of this work.

These late times are not strictly in keeping with the assumptions made in SYNOW. However, because past Day +100 permitted lines dominate the spectra of SNe Ia (Branch et al. 2008; Friesen et al. 2014), the SYNOW-like assumptions are not invalid at these epochs, although we do make allowance for the variation of the 'photosphere' with wavelength at these late times by modelling the blue and red regimes of the spectra with different $v_{\rm phot}$ values. We note that SYNOW-like assumptions lead to qualitative insights even at very late times (Friesen et al. 2012). With that in mind, we go further in our analysis by examining spectra from these late epochs.

The upper-left panel of Fig. 4 shows the observed spectrum obtained on March 6 (Day +33.4) and the SYNOW model. The SYNOW model is now strongly affected by the underlying blackbody and lack of continuum transfer. It has several prominent features – Na I D absorption centred at 5700 Å, Mg I absorption centred at 5000 Å, Fe II absorption centred at 5000 and 6400 Å, and Ca II absorption centred at 8200 Å. The SYNOW spectrum includes lines of six ions: Na I, Mg I, Ca II, Fe II, Co II, and Ni II. A value of

Table 2. SYNOW parameters for near-maximum spectra models.

Date	v_{phot}	T_{bb}	T_{exe}	Near-maximum SYNOW parameters													
				Na I		Mg I		Mg II		Si II		Si III		S II		Ca II	
				τ	v_e	τ	v_e	τ	v_e	τ	v_e	τ	v_e	τ	v_e	τ	v_e
Feb 04(+2.3)	12	11	10	1 ± 0.1	2	–	–	2 ± 0.4	2	6 ± 0.6	2	1 ± 0.3	1	2.2 ± 0.2	2	–	–
Feb 05(+3.3)	12	11	10	1 ± 0.1	2	2 ± 0.2	2	2 ± 0.4	2	6 ± 0.6	2	1 ± 0.3	1	1.2 ± 0.1	2	30 ± 6	3
Feb 06(+4.2)	12	11	10	10 ± 1	2	5 ± 0.5	2	2 ± 0.4	2	6 ± 0.6	2	1 ± 0.3	1	1.2 ± 0.1	2	–	–
Feb 12(+10.5)	12	11	10	1 ± 0.1	2	6 ± 0.5	2	0	2	6 ± 0.6	2	0	1	0.3 ± 0.1	2	180 ± 40	3
Feb 14(+12.4)	11	22	10	1 ± 0.1	2	3 ± 0.3	2	2 ± 0.4	2	4 ± 0.4	2	10 ± 3	1	0	2	–	–

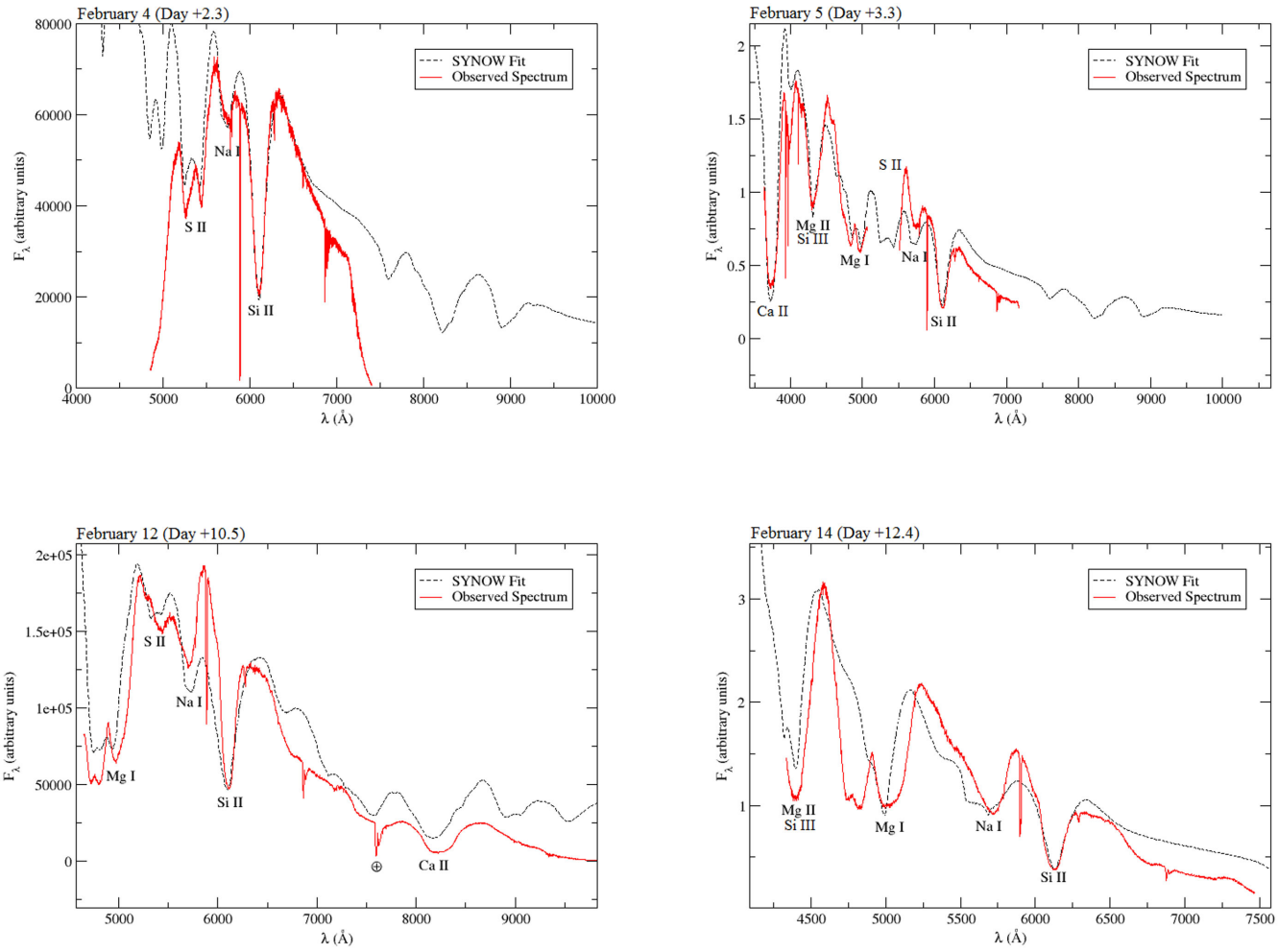

Figure 2. The observed spectra and SYNOW models representative of the near-maximum epoch. The upper-left panel shows the February 4 (Day +2.3) spectra, the upper-right panel shows the February 5 (Day +3.3) spectra, the lower-left panel shows the February 12 (Day +10.5) spectra, and the lower-right panel shows the February 14 (Day +12.4) spectra.

Table 3. SYNOW Parameters for post-maximum spectra.

Date	v_{phot}	T_{bb}	T_{exe}	Post-maximum SYNOW parameters													
				Na I		Mg I		Mg II		Si II		Si III		Ca II		Fe II	
				τ	v_e	τ	v_e	τ	v_e	τ	v_e	τ	v_e	τ	v_e	τ	v_e
Feb 19(+17.4)	11	22	10	2.5 ± 0.3	2	3 ± 0.3	2	6 ± 1.2	2	12 ± 1.2	1	10 ± 3	1	200 ± 50	3	0	2
Feb 20(+18.3)	11	22	10	2.5 ± 0.3	2	3 ± 0.3	2	4 ± 0.8	2	10 ± 1	1	10 ± 3	1	180 ± 40	3	0	2
Feb 21(+19.5)	11	22	10	2.5 ± 0.3	2	3 ± 0.3	2	3 ± 0.6	2	10 ± 1	1	10 ± 3	1	180 ± 40	3	3 ± 0.8	2
Feb 24(+22.5)	10	22	10	2.5 ± 0.3	2	3 ± 0.3	2	1 ± 0.2	2	10 ± 1	1	10 ± 3	1	140 ± 35	3	6 ± 1.5	2
Feb 26(+24.5)	10	22	10	2 ± 0.2	2	3 ± 0.3	2	2 ± 0.4	2	12 ± 1.2	1	14 ± 4	1	140 ± 35	3	6 ± 1.5	2

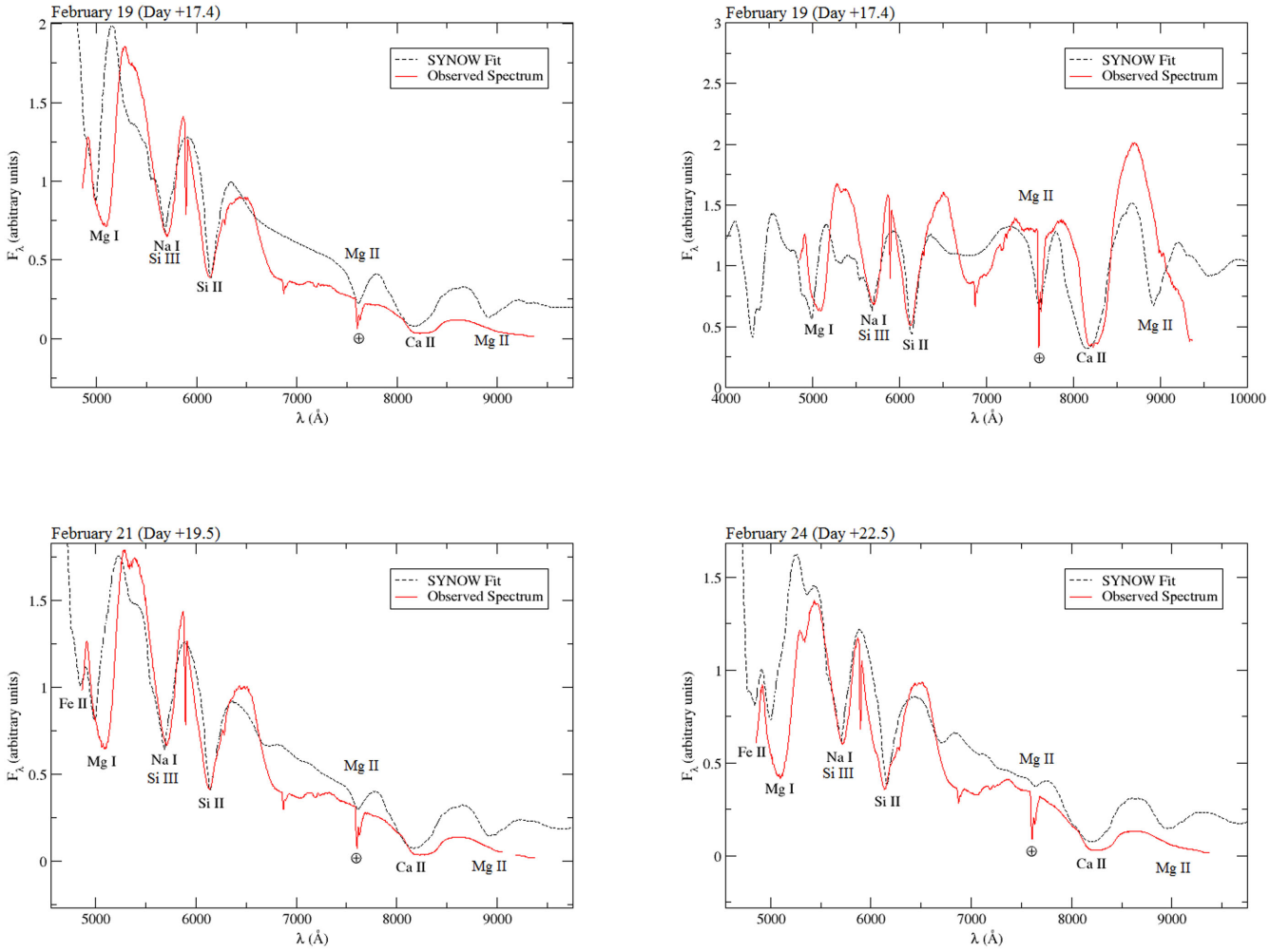

Figure 3. The observed spectra and SYNOW models representative of the post-maximum epoch. The upper-left panel shows the February 19 (Day +17.4) spectra, the upper-right panel shows the flattened February 19 (Day +17.4) spectra, the lower-left panel shows the February 21 (Day +19.5) spectra, and the lower-right panel shows the February 24 (Day +22.5) spectra.

Table 4. SYNOW parameters for late spectra models.

Date	$v_{\rm phot}$	$T_{\rm bb}$	$T_{\rm exe}$	Late SYNOW parameters													
				Na I		Mg I		Mg II		Ca II		Fe II		Co II		Ni II	
				τ	v_e	τ	v_e	τ	v_e	τ	v_e	τ	v_e	τ	v_e	τ	v_e
March 06(+33.4)	9	14	10	2 ± 0.2	2	3 ± 0.3	2	0	2	130 ± 30	3	6 ± 1.5	2	15 ± 4	3	10 ± 3.5	2
March 07(+34.4)	9	14	10	2 ± 0.2	2	3 ± 0.3	2	0	2	100 ± 25	3	6 ± 1.5	2	15 ± 4	3	10 ± 3.5	2
March 12(+39.1)	9	8	10	2 ± 0.2	2	0	2	0	2	100 ± 25	3	9 ± 2	2	15 ± 4	3	10 ± 3.5	2
March 17(+44.4)	9	8	10	3 ± 0.3	2	0	2	0	2	100 ± 25	3	15 ± 3.5	2	15 ± 4	2	10 ± 3.5	2
April 08(+66.2)	8	8	06	3 ± 0.3	2	0	2	0	2	250 ± 65	3	60 ± 15	2	15 ± 4	2	15 ± 5	2
May 08(+96.2)	6	8	06	30 ± 4	2	40 ± 5	2	30 ± 7	2	900 ± 300	3	50 ± 13	2	15 ± 4	2	0	2
May 09(+97.2)	6	8	06	60 ± 8	2	40 ± 5	2	–	–	900 ± 300	3	40 ± 10	2	35 ± 10	2	0	2
May 11(+99.1)	6	6	06	30 ± 4	2	35 ± 5	2	–	–	20 ± 4	3	15 ± 3.5	2	20 ± 5	2	0	2

$v_{\rm phot} = 9000$ kms^{-1} is used. A complete list of input parameters can be found in Table 4.

The upper-right panel of Fig. 4 shows the observed spectrum obtained on March 17 (Day +44.4) and the SYNOW model. It has several prominent features – Na I absorption centred at 5700 Å, Fe II and Co II absorption centred at 5000 and 6400 Å, and Ca II absorption centred at 8200 Å. The SYNOW spectrum includes lines of five ions: Na I, Ca II, Fe II, Co II, and Ni II.

The lower-left and lower-right panels of Fig. 4 show the observed spectrum obtained on May 8 (Day +96.2) and the SYNOW model over two wavelength regimes. $T_e = 6000$ K is used. Note that the two figures are split at 8000 Å. For the left-hand figure, $v_{\rm phot} = 9000$ kms^{-1} is used, whereas for the right-hand figure a much slower $v_{\rm phot}$ of 2000 kms^{-1} is used, and $v_e = 4$ is used for Ca II; otherwise it uses the same parameters as that shown on the left. Our use of a blackbody as the inner boundary condition, coupled with the fact

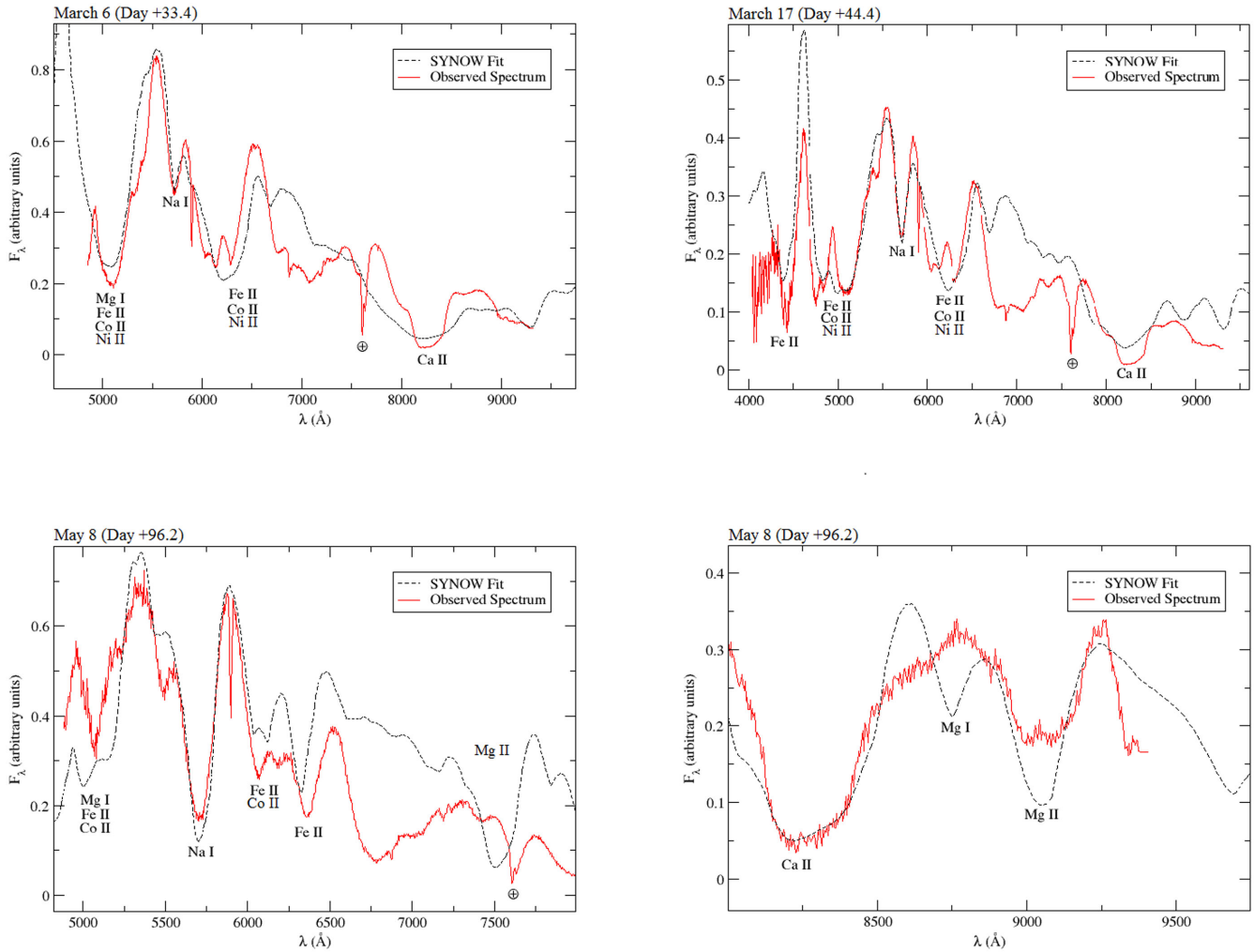

Figure 4. The observed spectra and SYNOW models representative of the late epoch. The upper-left panel shows the March 6 (Day +33.4) spectra, the upper-right panel shows the March 17 (Day +44.4) spectra, and the lower-left and lower-right panels show the May 8 (Day +96.2) spectra, split into two wavelength regimes.

that SYNOW does no continuum transfer and is a pure Schuster–Schwarzschild method leads to a bump in the pseudo-continuum or line features just to the blue of 7000 Å, this feature becomes even more pronounced at later epochs. The blue model continues to show Na D absorption centred at 5700 Å, Mg II absorption centred at 7600 and 8900 Å, Fe II absorption centred at 5000 Å and 6400 Å, and Ca II absorption centred at 8200 Å. The SYNOW spectrum includes lines of six ions: Na I, Mg I, Mg II, Ca II, Fe II, Co II, and Ni II.

6 PHOTOSPHERIC VELOCITY COMPARISONS

Fig. 5 shows the photospheric velocities of three supernovae: SN 1994D (Branch et al. 2005), SN 2014J (this work; Paper I; Ashall et al. 2014), and SN 2011fe (Parrent et al. 2012; Mazzali et al. 2014) versus time. The photospheric velocities of SN 2014J and SN 1994D decrease at a similar rate, although SN 2014J maintains a photospheric velocity about 1000 kms^{-1} faster than SN 1994D. The photospheric velocity of SN2011fe, on the other hand, decreases at a much faster rate, dropping from 15 000 to 8000 kms^{-1} in only 14 d. The velocity evolution of abundance tomography of SN 2011fe is similar to that found with SYNOW (Parrent et al. 2012; Mazzali et al. 2014), but that of SN 2014J is somewhat faster than found with SYNOW (Ashall et al. 2014). To a large extent the photospheric velocity and the density slope are degenerate so a shallow density slope can be traded off for a lower photospheric velocity. The slope of the P Cygni feature from peak to tail can be used to break this degeneracy, but only if one is sure that blending is not important (Baron et al. 1995; Baron, Hauschildt & Mezzacappa 1996).

Fig. 5 also shows the velocities of the ions obtained in Paper I. The results are in good agreement. Paper I finds high-velocity features of Fe II and Ca H+K at early times with Si II λ6355, λ5972, λ4130 match the photosphere well (being a little bit slower than inferred by SYNOW, until the photosphere recedes below the region of primary silicon formation. The trend is similar for the S II lines, although they were measured to be marginally slower than the Si II lines. The Mg II lines and the Ca IR triplet lines match the early photosphere very well, until hanging up as the photosphere recedes. The evolution of Fe II lines is that at early epochs that show a high-velocity component, match well the inferred SYNOW photosphere at about +20 d, fall significantly below the inferred SYNOW photosphere in the +40–50 d epochs, and then rise again to roughly match the inferred photosphere at Day +100. The variation gives an estimate of the error in inferring ion velocities purely observationally

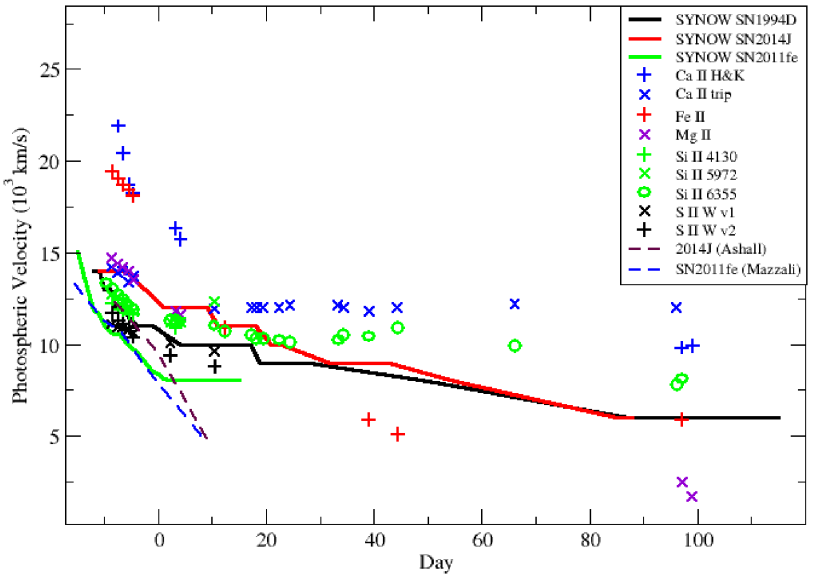

Figure 5. The photospheric velocities of three supernovae: SN 1994D (Branch et al. 2005), SN 2014J (this work; Paper I; Ashall et al. 2014), and SN 2011fe (Parrent et al. 2012; Mazzali et al. 2014) versus time. The SYNOW model velocity for SN 1994D (Branch et al. 2005) is shown in black, the SYNOW model velocity for SN 2014J (this work) is shown in red, SN 2014J (Ashall et al. 2014) is shown in maroon, the SYNOW model velocity for SN 2011fe (Parrent et al. 2012) is shown in green, and SN 2011fe (Mazzali et al. 2014) is shown in blue. The points show the observed line velocities taken from table 2 of Paper I.

and via a SYNOW approach. While we find a constant photosphere velocity at early times, Paper I finds that the strong lines such as Si II λ6355 decrease with time. This is not in contradiction, since strong resonance lines can extend to high velocities at early times, when the density is high in the outer ejecta.

7 COMPARISON WITH SN 2011Fe

SN 2011fe is also a nearby and well-studied Type Ia supernova. Here, we briefly discuss to what extent a comparison between SNe 2014J and SN 2011fe properties allow us to infer properties about their progenitors and explosion mechanism, although a complete study is beyond the scope of this paper. SN 2014J and SN 2011fe have similar maximum magnitudes, for example, in B SN 2014J: -19.19 ± 0.1 (Marion et al. 2015), -19.26 ± 0.1 (Kawabata et al. 2014); 2011fe: -19.21 ± 0.1 (Richmond & Smith 2012), -19.45 ± 0.08 (Tammann & Reindl 2013), and post-maximum decline rates Δm_{15}, SN 2014J: 1.06 ± 0.06, averaging the reported values (Ashall et al. 2014; Kawabata et al. 2014; Tsvetkov et al. 2014; Marion et al. 2015); SN 2011fe: 1.11 ± 0.07 (Richmond & Smith 2012; Pereira et al. 2013; McClelland et al. 2013; Tammann & Reindl 2013) and different line and photospheric velocities, up to 1500 kms^{-1} around maximum, as shown in Fig 5. Neither SN 2011fe nor SN 2014J show traces of a single degenerate companion (Lundqvist et al. 2015, but see also Graham et al. 2015) favouring, in principle, the double degenerate scenario (see also Soker, García-Berro & Althaus 2014; Soker 2015). SN 2014J is highly reddened $E(B-V) = 1.2$ (Goobar et al. 2014), while SN 2011fe is not, $E(B-V) = 0.03$ (Mazzali et al. 2014). Observed properties of both supernovae can be explained by the delayed-detonation explosion of a carbon–oxygen white dwarf (WD) with a mass close to the Chandrasekhar mass. In delayed-detonation explosion models (Khokhlov 1991; Hoeflich, Khokhlov & Wheeler 1995; Hoeflich & Khokhlov 1996), the main properties for the outcome are (Hoeflich et al. 2010): the composition of the WD – related to the WD progenitors; the central explosion ignition density – related with the accretion rate and/or, in the case of rotation, the time-scale of angular momentum loss; and the transition density from deflagration to detonation – the main factor that determines the ^{56}Ni mass, which is a free parameter. To reproduce the light curves, ^{56}Ni masses above 0.51–0.55 and 0.6–0.65 $M_\odot$ for SNe 2011fe and SN 2014J, respectively, have been estimated (Isern et al. 2013; Baron et al. 2015). Higher transition densities (lower pre-expansions) will produce more ^{56}Ni and less intermediate mass elements, but the corresponding increase in the kinetic energy would be above a factor of 5 smaller than the increase in ^{56}Ni masses. The difference in ejecta velocities between SNe 2014J and 2011fe is $\Delta v_{\rm ej} \sim 1500$ kms^{-1}, and the ejecta velocity is $v_{\rm ej} \sim 10\,000$ kms^{-1}, and so the difference is ∼15 per cent. The difference in ^{56}Ni mass between SNe 2014J and 2011fe is $\Delta M_{^{56}\rm Ni} \sim 0.1$, and the nickel mass is $M_{^{56}\rm Ni} \sim 0.6$, and so the difference is ∼17 per cent, therefore the difference in ejecta velocity should be more like 3 per cent if a variation in the transition density alone were the underlying physical difference between SNe 2014J and 2011fe. In fact, this is the reason why delayed-detonation models reproduce the Phillips relation: when the transition density is modified, different ^{56}Ni masses are obtained for similar kinetic energy, produced ad hoc, with pre-deflagrations, or via other models. See for example Hoeflich & Khokhlov (1996), (their table 1), for a delayed-detonation model denoted M36 that produces 0.6 $M_\odot$ of ^{56}Ni. A smaller transition density (model M37) changes ^{56}Ni by 16 per cent and $E_{\rm kin}$ by only 2 per cent.

This implies that the differences in the ejecta velocities of SN 2014J with respect to SN 2011fe cannot be explained by just increasing the transition density. The observed variation in velocities can possibly be explained assuming different central ignition densities or different WD chemical compositions, mainly the ratio C/O (Domínguez, Hoeflich & Straniero 2001b).

Smaller central ignition densities produce more ^{56}Ni and less neutronized elements in the central regions and, for smaller central densities, the WD binding energy is also smaller and so, the kinetic energy is higher, while maximum magnitudes and decline rates could be similar for the density range needed to explain these two

supernovae. Thus, SN 2014J could have been ignited at a central density smaller than that for SN 2011fe, due to a higher accretion rate or, in case of rotation, to a shorter time-scale for the angular momentum losses (Piersanti et al. 2003; Domínguez et al. 2006). If this was the case, the light curve tail of SN 2011fe would be dimmer than that of SN 2014J, as it seems to be in *B* band and less markedly in *V* (Foley et al. 2014), although late observations in the optical of SN 2014J have not yet been published. A greater C/O ratio will produce more ^{56}Ni and more kinetic energy. In fact, an increase of C/O above 20 per cent will produce an increase above 10 per cent in ^{56}Ni mass, an increase above 1500 kms^{-1} in line velocities and 2000 kms^{-1} in the photospheric velocity (Domínguez et al. 2001b). If the difference is due to the differences in the C/O ratio between the progenitors of SN 2014J and SN 2011fe, their light-curve tails will be similar – for the range in C/O needed to explain the observed velocities – and SN 2014J will be 0.1 mag brighter at maximum light. Tail brightness (we mean here more than 40 d after maximum) reflects the total ^{56}Ni mass, for SN 2011fe we interpret the slightly dimmer tail, as less ^{56}Ni mass ($\sim$0.1 $M_\odot$). At the same time the overall velocities are smaller, while the maximum magnitude and decline rate Δm_{15} are similar. For a higher central density, the kinetic energy is smaller due to the higher binding energies and electron captures are favoured, producing neutronized elements at the centre. Thus, less ^{56}Ni is produced (in agreement with the light curve, 35–40 d after maximum), but this ^{56}Ni is located closer to the surface, so at maximum the ^{56}Ni decrease is compensated by its more external location. Secondly, for these two SNe we know the distance. In SNe Ia at unknown distance, we should work with the 'peak to tail ratio' and then the uncertainty in the maximum magnitude would be critical (see Hoeflich et al. 2010). Reported observations show that SN 2014J is dimmer at maximum than SN 2011fe, but note that 0.1 mag is within the errors, SN 2014J is heavily reddened and there are discrepancies in the maximum magnitude as derived by different authors. The chemical composition of the exploding WD is related to the properties of the WD progenitors, mainly the initial main sequence mass and, to a smaller extent, the initial metallicity.

Assuming that both WDs are produced in the double degenerate scenario, a decrease of in C/O above 20 per cent are expected just by changing the initial accreting WD mass from 0.8 to 0.9 $M_\odot$, corresponding to the C + O cores of main-sequence masses 5 and 6 $M_\odot$ (initial solar composition) and up to 35 per cent, if a 1 $M_\odot$ WD (initial main-sequence mass 7 $M_\odot$) is considered (Bravo et al. 2010). Smaller differences, in terms of ^{56}Ni masses, would be obtained assuming different WD cooling times, diffusion and crystallization processes, before accretion, for example, an increase of 7 per cent in ^{56}Ni mass increasing the cooling time from 0.6 to 0.8 Gyr, (Bravo et al. 2011) or changing the metallicity (Bravo et al. 2010), i.e. from solar to sub-solar metallicities, as suggested for SN 2011fe (Mazzali et al. 2014; Baron et al. 2015). In both cases, the reason is the central abundance of ^{22}Ne that changes the neutronization and so, the nucleosynthesis (less ^{22}Ne, less neutronization and more ^{56}Ni), but the corresponding changes in kinetic energy/velocities would be smaller than in the previous cases, that is due to varying the C/O ratio or the central density. We note that the C/O ratio was studied in 3D in the context of pure deflagration models by Röpke & Hillebrandt (2004), who did not find a significant variation in the total mass of ^{56}Ni produced in their simulations with their particular burning prescription. Further work by this same group extending to the case of delayed-detonation models; however, found complete agreement with the work of Domínguez, Hoeflich & Straniero (2001a) and Hoeflich et al. (2010), that is they found the above effects of the C/O ratio on the mass of ^{56}Ni produced.

In summary, it may be that SN 2014J comes from a smaller primary (and corresponding main sequence) WD mass compared to SN 2011fe, explaining the different observed velocities at maximum, for similar decline rates. In this case, similar light-curve tail brightnesses would be expected for the range of C/O needed. If the observed maximum magnitude for both SNe were correct and SN 2014J is slightly dimmer at maximum, but showing a brighter light-curve tail than SN 2011fe (to be confirmed), it is more likely that SN 2011fe had a greater central ignition density than SN 2014J, this would also explain the smaller expansion velocities of 2011fe. For SN 2011fe, a sub-solar metallicity, about $Z_\odot/20$, has been suggested (Mazzali et al. 2014; Baron et al. 2015). If SN 2011fe has a lower progenitor metallicity than that of SN 2014J, SN 2011fe would be expected to be brighter than SN 2014J, everything else being equal. However, this would slightly increase its maximum magnitude. The metallicity difference between SN 2011fe and SN 2014J is likely small, therefore it would not cause significant variations in the brightness at maximum light.

8 DISCUSSION AND CONCLUSIONS

Ashall et al. (2014) performed a different type of spectral analysis on SN 2014J and it is worthwhile to compare the results of the two methods. We are in fact mostly in agreement with the conclusions of Ashall et al. (2014), but we differ in some cases and we discuss where we agree and disagree. We do not calculate abundances to compare with Ashall et al. (2014), since in SYNOW the excitation temperature is just a modelling parameter. While the early spectra show clear evidence for standard SNe Ia features, we do not find carbon in the spectra, nor do we find oxygen, both of which were found by Ashall et al. (2014) at early times. We also do not find strong evidence for mixing of nickel to high velocities. We find weak evidence for Si III post-maximum (up to Day 23) and Ashall et al. (2014) find no evidence for Si III after Day −7 (Jan 27). The evidence for Si III is not very strong, though, so this difference is not significant. The general results from *INTEGRAL*, which detected the 847 and 1238 keV γ-ray lines of radioactive ^{56}Co (Churazov et al. 2014, 2015; Diehl et al. 2014, 2015), showed that the general nickel distribution was stratified with a total ^{56}Ni mass of $\sim$0.5 $M_\odot$. Due to the low signal to noise, there is some ambiguity about just how to interpret the results, that is, whether the γ-rays favour symmetric nickel distributions (Churazov et al. 2014, 2015) or whether the lines are significantly Doppler-broadened asymmetric ones (Diehl et al. 2014, 2015). We are not terribly sensitive to small asymmetries, and therefore we cannot distinguish between these different interpretations. However, our results are in general agreement with the underlying ^{56}Ni distribution inferred from the *INTEGRAL* data.

While abundance tomography (Ashall et al. 2014) indicates the presence of significant oxygen, at early times, we do not find any spectroscopic signatures for oxygen at early times and can only weakly identify it at late times. Mg II models the P Cygni profile around 4350 Å in the early and the near-maximum spectra, while O I does not. While Mg II does not have the same strong identifying feature at 4350 Å in the post-maximum spectra, it does model the 7600 feature decently well, while adding O I causes an absorption a hundred or so angstroms too blue unless O I is constrained to be within 1000 kms^{-1} of the photospheric velocity. This is illustrated in Fig. 6. It seems odd that O I would be confined to a region so close to the photosphere even though the photosphere has moved from 14 000 to 6000 kms^{-1}.

There is some reason to doubt the Mg II identification, though, as post-maximum spectra do not show a strong feature at Mg II λλ9226,

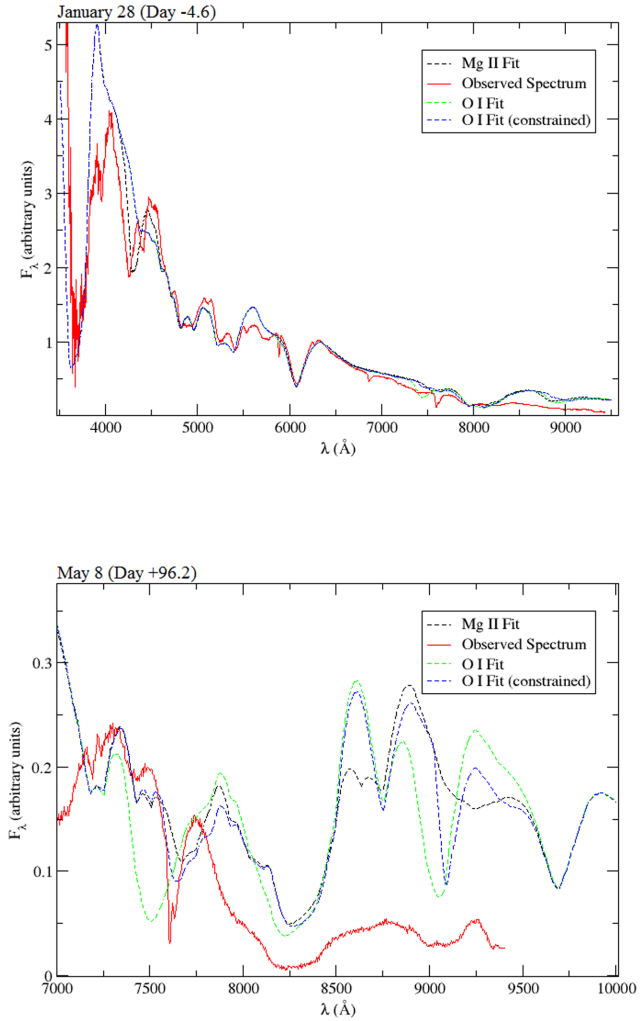

Figure 6. Comparison between Mg II and O I in the synthetic spectra. The upper panel shows an early spectrum (Day −4.6), which emphasizes the need for Mg II to model the absorption feature near 4300 Å. The lower panel shows a late spectrum (Day +96.2). While Mg II models the 7600 feature decently well, the O I absorption in this region is far too blue unless oxygen is constrained to a maximum velocity a mere 1000 km s^{-1} above the photospheric velocity. It is worth noting, though, that the O I absorption near 9100 Å does seem to model a feature of the observed spectrum, so we acknowledge the possible presence of oxygen at late times.

and the O I feature does seem to correspond the absorption at 9100 Å somewhat. As such, and considering SYNOW's limited applicability at late times, we cannot confidently rule out the presence of oxygen at late times. Also, the O I identification is a bit suspect since the O I 7774 line is modelled well by the constrained ion, the 9100 Å feature is perhaps better modelled by the unconstrained ion. Thus, we should be careful about drawing conclusions about mixing of unprocessed or only slightly processed elements to low velocities.

Just because there is little spectroscopic evidence for oxygen does not mean that it is not there. Since O I has an ionization potential for 13.6 eV, it requires higher temperatures to populate the excited states and so at low temperatures oxygen can be spectroscopically hidden. However, we also do not find any evidence for mixing of ^{56}Ni to high velocities. One would expect that if radioactive ^{56}Ni is mixed to high velocities, then non-thermal excitation of oxygen from fast electrons created by γ-ray interactions should be available to excite and ionize significant amounts of oxygen, which leads to strong O I lines. We assume the spectroscopic rule of thumb that the strongest lines of most ions come usually when it is not the dominant ion, but rather when the next ionization state is dominant. This is true because then there is plenty of energy to populate the excited states of the lower ionization stage.

Within the limits of our analysis, we show that there is not significant oxygen in the observed spectra and that there appears to be no need for significant mixing of ^{56}Ni into the outer layers of SN 2014J. We find good agreement with the photospheric velocity from other groups using a similar approach, particularly with Paper I. The fast decline found in the photospheric velocity by Ashall et al. (2014) is likely due to a difference in definition of the photosphere, due to their Monte Carlo approach rather than some important systematic difference in the methods, but the difference in definition is important to keep in mind when comparing velocities determined by different methods. The evidence that the definitions are different can be seen in Fig. 5, where the trend in velocities of Si II λ6355 found by Ashall et al. (2014) follow those that were strictly measured from the spectra in Paper I.

The late-time spectra shown in Fig. 4 are in good general agreement with the more detailed modelling results in the IR (Friesen et al. 2014) and in the mid-IR (Telesco et al. 2015). In general, we find features dominated by iron-group elements, with features from intermediate-group elements such as Ca II and Mg II whose lines become strong at low temperatures. That is, we find evidence for a layered structure that is generically predicted by delayed-detonation and pulsating delayed-detonation models.

In conclusion, our SYNOW modelling indicates that 2014J is a relatively normal SN Ia. Si II, S II, Mg II, and Ca II features dominate the spectra at early times. These ions are joined by Na I and Mg I as we approach maximum light, and at later times iron-group elements also appear, as expected in the stratified abundance model of the formation of normal Type Ia SNe. We generally agree with the findings of Ashall et al. (2014), but while abundance tomography indicates the presence of significant oxygen at early epochs, we do not find strong evidence to support this, as we find no spectroscopic signatures for oxygen at early times and only very weak signatures at late times. By strong evidence, we see no evidence for the need for the O I 7774 line, despite the fact that there is a telluric feature. In normal SNe Ia, the O I 7774 is quite evident even with the telluric feature (see Branch et al. 2005). Using our results and other published results, we are able to account for the similarities and differences between SN 2014J and SN 2011fe.

ACKNOWLEDGEMENTS

This work is based on service observations (programme SW2013a08, PI P- Ruiz-Lapuente) made with the William Herschel Telescope (WHT), and on discretionary observations made with the Isaac Newton Telescope (INT), both operated on the island of La Palma by the Isaac Newton Group (ING) in the Spanish Observatorio del Roque de los Muchachos of the Instituto de Astrofísica de Canarias. We thank the ING Director for having made public the INT data as soon as they were obtained. We also acknowledge the observers who kindly donated their time to monitor SN2014J on both the WHT and the INT. We thank Mercedes Molla for the proposal of observation time. The work has been supported in part by support for programme HST-GO-12948.004-A provided by NASA through a grant from the Space Telescope Science Institute, which is operated by the Association of Universities for Research in Astronomy, Incorporated, under NASA contract NAS5-26555. EB acknowledges

support from a Carl Bush Fellowship from the University of Oklahoma. Support for LG is provided by the Ministry of Economy, Development, and Tourism's Millennium Science Initiative through grant IC120009, awarded to The Millennium Institute of Astrophysics, MAS. LG acknowledges support by CONICYT through FONDECYT grant 3140566. JIGH acknowledges financial support from the Spanish Ministry of Economy and Competitiveness (MINECO) under the 2011 Severo Ochoa programme MINECO SEV-2011-0187, and the 2013 Ramón y Cajal programme MINECO RYC-2013-14875, and the Spanish ministry project MINECO AYA2014-56359-P. ID acknowledges MINECO-FEDER grant AYA2011-22460.

REFERENCES

Amanullah R. et al., 2014, ApJ, 788, L21
Ashall C., Mazzali P., Bersier D., Hachinger S., Phillips M., Percival S., James P., Maguire K., 2014, MNRAS, 445, 4427
Baron E. et al., 1995, ApJ, 441, 170
Baron E., Hauschildt P. H., Mezzacappa A., 1996, MNRAS, 278, 763
Baron E. et al., 2015, MNRAS, 454, 2549
Branch D., Baron E., Jeffery D. J., 2003, in Weiler K. W., ed., Supernovae and Gamma-Ray Bursts. Springer-Verlag, New York, p. 47
Branch D. et al., 2004, ApJ, 606, 413
Branch D., Baron E., Hall N., Melakayil M., Parrent J., 2005, PASP, 117, 545
Branch D. et al., 2007, PASP, 119, 709
Branch D. et al., 2008, PASP, 120, 135
Bravo E., Domínguez I., Badenes C., Piersanti L., Straniero O., 2010, ApJ, 711, L66
Bravo E., Althaus L. G., García-Berro E., Domínguez I., 2011, A&A, 526, A26
Churazov E. et al., 2014, Nature, 512, 406
Churazov E. et al., 2015, ApJ, 812, 62
Diehl R. et al., 2014, Science, 345, 1162
Diehl R. et al., 2015, A&A, 574, A72
Domínguez I., Hoeflich P., Straniero O., 2001a, ApJ, 557, 279
Domínguez I., Hoeflich P., Straniero O., 2001b, Nucl. Phys. A, 688, 21
Domínguez I., Piersanti L., Bravo E., Tornambé A., Straniero O., Gagliardi S., 2006, ApJ, 644, 21
Foley R. J. et al., 2014, MNRAS, 443, 2887
Friesen B., Baron E., Branch D., Chen B., Parrent J. T., Thomas R. C., 2012, ApJS, 203, 12
Friesen B., Baron E., Wisniewski J. P., Parrent J. T., Thomas R. C., Miller T. R., Marion G. H., 2014, ApJ, 792, 120
Galbany L. et al., 2016, MNRAS, 457, 525 (Paper I)
Goobar A. et al., 2014, ApJ, 784, L12
Graham M. L. et al., 2015, ApJ, 801, 136
Hillebrandt W., Kromer M., Röpke F. K., Ruiter A. J., 2013, Frontiers Phys., 8, 116
Hoeflich P., Khokhlov A., 1996, ApJ, 457, 500
Hoeflich P., Khokhlov A. M., Wheeler J. C., 1995, ApJ, 444, 831
Hoeflich P. et al., 2010, ApJ, 710, 444
Isern J. et al., 2013, A&A, 552, A97
Jack D., Baron E., Hauschildt P. H., 2015, MNRAS, 449, 3581
Jeffery D., Branch D., 1990, in Wheeler J. C., Piran T., eds, Supernovae. World Scientific, Singapore, p. 149
Jeffery D. J., Ketchum W., Branch D., Baron E., Elmhamdi A., Danziger I. J., 2007, ApJS, 171, 493
Johansson J. et al., 2014, MNRAS, preprint (astro-ph/1411.3332)
Kawabata K. S. et al., 2014, ApJ, 795, L4
Kelly P. L. et al., 2014, ApJ, 790, 3
Khokhlov A., 1991, A&A, 245, 114
Lundqvist P. et al., 2015, A&A, 577, A39
McClelland C. M., Garnavich P. M., Milne P. A., Shappee B. J., Pogge R. W., 2013, ApJ, 767, 119
Maoz D., Mannucci F., Nelemans G., 2014, ARA&A, 52, 107
Margutti R., Parrent J., Kamble A., Soderberg A. M., Foley R. J., Milisavljevic D., Drout M. R., Kirshner R., 2014, ApJ, 790, 52
Marion G. H. et al., 2015, ApJ, 798, 39
Mazzali P. A. et al., 2014, MNRAS, 439, 1959
Mihalas D., 1978, Stellar Atmospheres. W. H. Freeman, New York
Nielsen M. T. B., Gilfanov M., Bogdán Á., Woods T. E., Nelemans G., 2014, MNRAS, 442, 3400
Parrent J. T. et al., 2012, ApJ, 752, L26
Parrent J., Friesen B., Parthasarathy M., 2014, Ap&SS, 351, 1
Pereira R. et al., 2013, A&A, 554, A27
Pérez-Torres M. A. et al., 2014, ApJ, 792, 38
Piersanti L., Gagliardi S., Iben I., Jr, Tornambé A., 2003, ApJ, 583, 885
Richmond M. W., Smith H. A., 2012, J. Am. Assoc. Var. Star Obs., 40, 872
Ritchey A. M., Welty D. E., Dahlstrom J. A., York D. G., 2015, ApJ, 799, 197
Röpke F. K., Hillebrandt W., 2004, A&A, 420, L1
Ruiz-Lapuente P., 2014, New Astron. Rev., 62, 15
Siverd R. J., Goobar A., Stassun K. G., Pepper J., 2015, ApJ, 799, 105
Soker N., 2015, MNRAS, 450, 1333
Soker N., García-Berro E., Althaus L. G., 2014, MNRAS, 437, L66
Tammann G. A., Reindl B., 2013, A&A, 549, A136
Telesco C. M. et al., 2015, ApJ, 798, 93
Tsvetkov D. Y., Metlov V. G., Shugarov S. Y., Tarasova T. N., Pavlyuk N. N., 2014, Contrib. Astron. Obs. Skalnaté Pleso, 44, 67
Welty D. E., Ritchey A. M., Dahlstrom J. A., York D. G., 2014, ApJ, 792, 106

This paper has been typeset from a TEX/LATEX file prepared by the author.